JM PAPERS

Effect of Stokes number and particle-to-fluid density ratio on turbulence modification in channel flows

P. Gualtieri[1], F. Battista[1],†, F. Salvadore[2] and C.M. Casciola[1]

[1]Department of Mechanical and Aerospace Engineering, Sapienza University of Rome, via Eudossiana 18, 00184 Rome, Italy

[2]HPC Department, CINECA, via dei Tizii 6/B, 00185 Rome, Italy

Two-way momentum-coupled direct numerical simulations of a particle-laden turbulent channel flow are addressed to investigate the effect of the particle Stokes number and of the particle-to-fluid density ratio on the turbulence modification. The exact regularised point-particle method is used to model the interphase momentum exchange in presence of solid boundaries, allowing the exploration of an extensive region of the parameter space. Results show that the particles increase the friction drag in the parameter space region considered, namely the Stokes number $St_+ \in [2, 80]$, and the particle-to-fluid density ratio $\rho_p/\rho_f \in [90, 5760]$ at a fixed mass loading $\phi = 0.4$. It is noteworthy that the highest drag occurs for small Stokes number particles. A measurable drag increase occurs for all particle-to-fluid density ratios, the effect being reduced significantly only at the highest value of ρ_p/ρ_f. The modified stress budget and turbulent kinetic energy equation provide the rationale behind the observed behaviour. The particles' extra stress causes an additional momentum flux towards the wall that modifies the structure of the buffer and of the viscous sublayer where the streamwise and wall-normal velocity fluctuations are increased. Indeed, in the viscous sublayer, additional turbulent kinetic energy is produced by the particles' back-reaction, resulting in a strong augmentation of the spatial energy flux towards the wall where the energy is ultimately dissipated. This behaviour explains the increase of friction drag in particle-laden wall-bounded flows.

Key words: particle/fluid flow

† Email address for correspondence: francesco.battista@uniroma1.it

1. Introduction

Turbulence modulation by inertial particles represents a challenging multiscale problem (Soldati & Marchioli 2009; Balachandar & Eaton 2010), whose full understanding would impact on a better comprehension of natural phenomena (Woods 2010; Fu *et al.* 2014), and technological applications ranging from industrial (Jenny, Roekaerts & Beishuizen 2012; Capecelatro, Pepiot & Desjardins 2014) to medical applications (Kleinstreuer & Zhang 2010).

Besides its relatively simple geometrical configuration, the turbulent flow in a channel still represents a paradigmatic problem in multiphase flows; see Marchioli, Picciotto & Soldati (2007), Sardina *et al.* (2012) and Fong, Amili & Coletti (2019). One of the major issues in wall turbulence is whether or not the presence of solid particles can modify the flow friction at the wall, and the overall structure of the turbulent fluctuations. Indeed, there are numerical studies that report drag reduction by particles (Vreman 2007; Zhao, Andersson & Gillissen 2010), while others report its increase, both numerically (Pan & Banerjee 1997; Costa, Brandt & Picano 2020, 2021) and experimentally (Righetti & Romano 2004; Li *et al.* 2012).

The lack of a clear answer can be ascribed to two main reasons. The first is represented by the multiscale interaction between turbulence and inertial particles that can be parametrised in terms of additional dimensionless parameters, i.e. the particle Reynolds number, the particle-to-fluid density ratio, the particle-to-fluid response time (i.e. the Stokes number), and the volume fraction of the suspensions; see Elgobashi (2006). At least a four-dimensional parameter space should be explored with experiments and/or numerical simulations to characterise the turbulence modification. The second reason concerns the different numerical approaches describing with different grades of accuracy the fluid–particle interaction; see e.g. the review by Brandt & Coletti (2022). Usually, a very accurate description of the fluid–particle interaction goes along with a tremendous computational cost. Resolved particle simulations have been applied to study the effect of almost neutrally buoyant suspensions and the modulation of wall turbulence of one specific particle population. However, when a wider range of the parameter space is spanned, the intrinsic scale separation calls for modelling the fluid–particle interaction in order to reduce the computational cost. When the flow past each particle is not actually resolved, the major interaction between the fluid and the point-particles consists of the momentum exchange (two-way coupling regime).

In the limit of small particle Reynolds number, and dilute volume fractions, the particle-source in cell method (Crowe, Sharma & Stock 1977) has been the first approach designed to capture the interphase momentum exchange. Since (Crowe *et al.* 1977), many alternative and more accurate approaches have been conceived – see, for instance, Garg *et al.* (2007), Horwitz & Mani (2016), Pakseresht, Esmaily & Apte (2020) and Evrard, Denner & van Wachem (2021) – in the context of Euler–Lagrangian simulations. Other authors filtered the fluid equations on the scale of the particle accounting for excluded volume effects, and the related subgrid stresses on the fluid (Capecelatro & Desjardins 2013; Ireland & Desjardins 2017). In the force coupling method (Maxey & Patel 2001; Lomholt & Maxey 2003; Yeo & Maxey 2010) and the pairwise interaction extended point-particle method (Akiki, Jackson & Balachandar 2017*a*; Akiki, Moore & Balachandar 2017*b*), the authors evaluated the local disturbance produced by the particles by solving a steady Stokes flow. In the exact regularised point-particle (ERPP) method (Gualtieri *et al.* 2015; Battista *et al.* 2019), and in the work by Balachandar, Liu & Lakhote (2019), the particle disturbance was modelled exploiting unsteady Stokes solutions. Other related

approaches adopt regularisation procedures based on nonlinear diffusion processes; see Poustis *et al.* (2019). All the above methods aimed to retrieve in a somehow lumped way the boundary condition that was killed when the particles were modelled as point masses (see Prosperetti 2015), still preserving an accurate and physically reliable description of the fluid–particle interaction. The ERPP method reproduces faithfully the momentum exchange between small particles and the carrier phase, and given its computational efficiency, it can be used to explore a wide range of the parameter space where turbulence modulation occurs at different grades.

This paper addresses the turbulence modulation in the range of Stokes number $St_+ \in [2, 80]$, and of particle-to-fluid density ratio $\rho_p/\rho_f \in [90, 5760]$ at a fixed mass loading $\phi = 0.4$. In this region of the parameter space, the overall friction drag is either increased or left unaltered. This behaviour is explained in terms of the particles' additional momentum transfer towards the wall, i.e. the particles' extra stress, and in terms of the modification of the turbulent kinetic energy (TKE) budget. As discussed by Capecelatro, Desjardins & Fox (2018), there exist regimes where TKE production due to the Reynolds shear stress (shear production) is overwhelmed by the particle feedback term (particle production). In homogeneous flows (Richter 2015; Gualtieri, Battista & Casciola 2017), this results in the increase of the fluid dissipation rate at the scales where additional kinetic energy is produced. In inhomogeneous conditions, however, these mechanisms originate a spatial energy flux. Indeed, in regimes where a strong increase of the friction drag is observed, the particle production term turns out to be the largest one and is localised near the wall. The excess of TKE produced by the particles is not locally dissipated and triggers an intense spatial energy flux towards the wall, where ultimately the energy is dissipated by the viscosity. This behaviour explains the increase of the friction drag and the concurrent increase of velocity fluctuations that are observed in the viscous sublayer in the presence of two-way coupling effects.

The paper is organised as follows. Section 2 summarises briefly the numerical approach based on the ERPP model, and discusses the simulations' parameters. Section 3 first documents the turbulence modulation and then explain it in terms of the alteration of the stress and TKE balances. Section 4 draws the main conclusions of the study.

2. Particle-laden turbulent channel flow

The dimensionless Navier–Stokes equations for a divergence-free velocity field,

$$\left.\begin{aligned}
\boldsymbol{\nabla} \cdot \boldsymbol{u} &= 0, \\
\frac{\partial \boldsymbol{u}}{\partial t} + \boldsymbol{\nabla} \cdot (\boldsymbol{u} \otimes \boldsymbol{u}) &= -\left.\frac{\mathrm{d}p}{\mathrm{d}x}\right|_0 \boldsymbol{e}_x - \boldsymbol{\nabla} p + \frac{1}{Re_b} \nabla^2 \boldsymbol{u} + \boldsymbol{f},
\end{aligned}\right\} \quad (2.1)$$

are solved in the domain $\mathcal{D} = [0, 4\pi] \times [0, 2\pi] \times [0, 2]$ in the streamwise (x), spanwise (y) and wall-normal (z) directions, respectively. Periodic boundary conditions are applied along the streamwise and spanwise directions, whilst no-slip boundary conditions are enforced at the channel's top and bottom walls. The flow is sustained by a constant mean pressure gradient $\mathrm{d}p/\mathrm{d}x|_0$ applied in the direction of the streamwise unit vector $\boldsymbol{e}_x$. The reference quantities are the fluid density ρ_f, the channel half-height h, the bulk velocity of the reference uncoupled case (no back-reaction on the fluid) $U_{b,0} = Q_0/(2h)$, where Q_0 is the flow rate per unit length, and the fluid viscosity μ. It follows that the Reynolds number is $Re_b = \rho_f U_{b,0} h/\mu$. In (2.1), field $\boldsymbol{f}$ represents the particle feedback on the fluid

as modelled by the ERPP approach, namely

$$f(x, t) = -\sum_{p=1}^{N_p} D_p(t - \epsilon)g[x - x_p(t - \epsilon), \epsilon] + \tilde{D}_p(t - \epsilon)g[x - \tilde{x}_p(t - \epsilon), \epsilon], \quad (2.2)$$

where the sum encompasses all N_p particles. The dimensionless drag force on the pth particle is $D_p = 3\pi d_p/Re_b\,(\hat{u}|_p - v_p)$, where d_p is the dimensionless particle diameter, v_p is the particle velocity, and $\hat{u}|_p = \hat{u}[x_p(t), t]$ is the fluid velocity at the particle position $x_p(t)$ deprived by the particle self-disturbance, i.e. the field that accounts for the turbulent background velocity and for the disturbance of all particles except the pth. This field is evaluated by summing the contributions of all the particles and by successively removing the particle self-disturbance that, in the context of the ERPP approach, is known in a closed analytical form.

In (2.2), the variables with a tilde denote quantities about the image particles obtained by reflection with respect to the wall according to $\tilde{x}_p^\pi = x_p^\pi, \tilde{x}_p^n = -x_p^n, \tilde{D}_p^\pi = D_p^\pi, \tilde{D}_p^n = -D_p^n$, where the superscripts π and n denote the coordinates along the tangent plane and the wall-normal direction, respectively. The image particle is a feature of the ERPP approach to account for the particle feedback in presence of solid boundaries. Both the current time t and the regularisation time scale ϵ_R are made dimensionless with $h/U_{b,0}$, namely $\epsilon = \epsilon_R U_{b,0}/h$. In the ERPP approach, the regularisation of the singular feedback force field caused by the particles in the fluid is achieved by exploiting the disturbance vorticity that each particle generates when subjected to force D_p. The disturbance vorticity is consistently regularised by the fluid viscosity, and its 'regular' counterpart forces the Navier–Stokes equations via the field $f(x, t)$ in (2.2). The delay time scale ϵ represents the time required by the vorticity generated by the particles to diffuse up to the grid size. It turns out that the Dirac delta functions that localise the force on the fluid at the particle position are turned on a physical ground into Gaussian functions, i.e. $g[x - x_p(t - \epsilon), \epsilon]$, centred at the delayed particle position $x_p(t - \epsilon)$ with variance given by the regularisation time scale ϵ; see e.g. Gualtieri *et al.* (2015) and Battista *et al.* (2019) for a more detailed description of the method.

Equations (2.1) are solved in Cartesian coordinates using an in-house developed code that exploits a hybrid MPI-GPUs parallelisation. Chorin's projection method (Chorin 1968) is used to enforce the divergence-free constraint imposed by the mass balance. Both convective and diffusive terms are discretised in space by second-order finite differences on a staggered grid, and are integrated explicitly in time using a third-order, four-stage, low-storage Runge–Kutta method.

Inner or wall units are provided by the viscous length $\ell_* = \nu/u_*$ (where $\nu = \mu/\rho_f$ is the kinematic viscosity) and the friction velocity $u_* = \sqrt{\tau_w/\rho_f}$ (where τ_w is the average wall shear stress). The wall-normal distance in inner units is denoted as $z_+ = z/\ell_*$, and the friction Reynolds number is $Re_* = u_*h/\nu$. All the simulations are performed with the same friction Reynolds number $Re_* = 185$. The bulk Reynolds number of the reference uncoupled case (no particle back-reaction) is $Re_b = 2890$. The discretisation grid is uniformly spaced in the streamwise and spanwise directions, while it is stretched along the wall-normal direction. The number of grid points and the grid spacing are reported in table 1.

Concerning the disperse phase, at a relatively large particle-to-fluid density ratio ρ_p/ρ_f, the only relevant hydrodynamic force acting on the particles is the Stokes drag; see Gatignol (1983) and Maxey & Riley (1983). Newton's equations for the particles read

Case	$N_x \times N_y \times N_z$	ρ_p/ρ_f	St_+	d_p^+	N_p
S2	$1152 \times 576 \times 168$	180	2	0.45	46 678 528
S3	$1024 \times 512 \times 168$	180	3	0.59	25 408 560
S5	$768 \times 384 \times 168$	180	5	0.71	11 808 832
S10	$768 \times 384 \times 168$	180	10	1	4 175 052
S15	$768 \times 384 \times 168$	180	15	1.23	2 272 612
S20	$768 \times 384 \times 168$	180	20	1.41	1 476 104
S40	$768 \times 384 \times 168$	180	40	2	521 880
S80	$768 \times 384 \times 168$	180	80	2.83	184 512
R90	$768 \times 384 \times 168$	90	10	1.41	2 952 208
R360	$768 \times 384 \times 168$	360	10	0.71	5 904 416
R720	$768 \times 384 \times 168$	720	10	0.5	8 350 104
R1440	$768 \times 384 \times 168$	1440	10	0.35	11 808 832
R2880	$768 \times 384 \times 168$	2880	10	0.25	16 700 224
R5760	$768 \times 384 \times 168$	5760	10	0.18	23 617 664

Table 1. All simulations are performed with the same mean pressure gradient corresponding to a friction Reynolds number $Re_* = 185$ and a bulk Reynolds number for the reference uncoupled case (one-way coupling, no back-reaction) $Re_b = 2890$. The grid resolution is $N_x \times N_y \times N_z$ in the dimensionless domain $\mathcal{D} = [0, 4\pi] \times [0, 2\pi] \times [0, 2]$. The grid spacing is uniform in the streamwise and spanwise directions corresponding to $\Delta x_+ = \Delta y_+ = 3$, $\Delta x_+ = \Delta y_+ = 2$ and $\Delta x_+ = \Delta y_+ = 1.5$ for the different grids. In the wall-normal direction, the grid is stretched corresponding to minimum spacing $\Delta z_+|_w = 0.2$ at the wall and $\Delta z_+|_0 = 3$ at the centreline. In all the simulations, the mass loading is $\phi = 0.4$. Here, ρ_p/ρ_f is the particle-to-fluid density ratio, $St_+ = \tau_p/\tau_*$ is the Stokes number in wall units, d_p^+ is the particle diameter in wall units, and N_p is the number of particles.

$$
\left.
\begin{aligned}
\frac{\mathrm{d}\boldsymbol{x}_p}{\mathrm{d}t} &= \boldsymbol{v}_p, \\
\frac{\mathrm{d}\boldsymbol{v}_p}{\mathrm{d}t} &= \frac{1}{St_b}(\hat{\boldsymbol{u}}|_p - \boldsymbol{v}_p),
\end{aligned}
\right\}
\tag{2.3}
$$

where the bulk Stokes number is $St_b = \tau_p/\tau_0 = Re_b \, \rho_p/(18\rho_f)(d_p/h)^2$, with $\tau_0 = h/U_{b,0}$, and τ_p the particle relaxation time. Equations (2.3) are integrated in time with the same four-stage, low-storage Runge–Kutta method used for the carrier phase. A purely elastic bounce is implemented at the channel's top and bottom walls. In some of the cases listed in table 1, namely for the largest Stokes numbers ($St_+ = 40, 80$) and for the relatively smaller density ratio ($\rho_p/\rho_f = 90$), companion simulations that included the Faxén correction (Gatignol 1983) were performed, showing inappreciable effects on the results, and they will not be discussed further here.

The dynamics of the two-way coupled system for small particle Reynolds number and dilute suspensions is controlled by a set of four dimensionless parameters, as it follows from the application of the Buckingham theorem, namely $\{Re_*; \; St_+; \; \rho_p/\rho_f; \; N_p\}$, where N_p is the total number of particles in the flow domain $\mathcal{D}$, and the inner-scale Stokes number is defined as $St_+ = \tau_p/\tau_* = St_b \, Re_*^2/Re_b$, with $\tau_* = \ell_*/u_*$ the friction time scale. However, N_p is a quantity that is difficult to determine experimentally. In contrast, the total mass of the disperse phase can be measured easily by a weight balance. Hence N_p can be replaced by the mass loading $\phi = N_p \rho_p V_p/\rho_f V_f = (\rho_p/\rho_f)N_p(d_p/h)^3/(96\pi)$, where V_p is the volume of the particle, and V_f is the volume of the fluid in the domain $\mathcal{D}$; see e.g. Elgobashi (2006) and Balachandar & Eaton (2010).

(*a*)   (*b*)
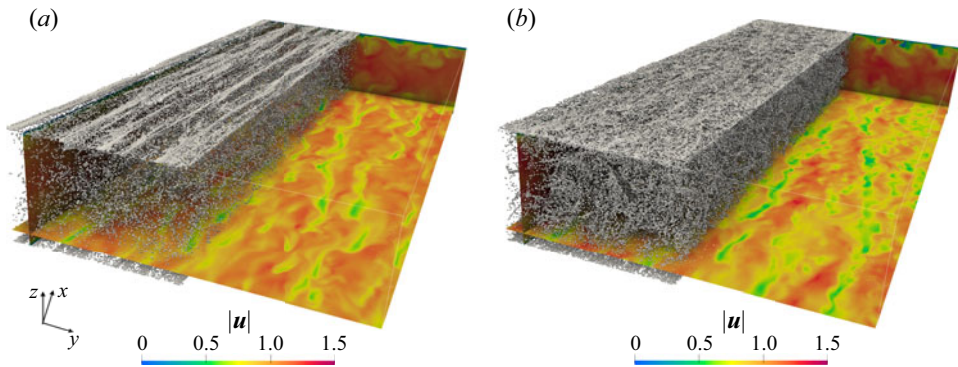

Figure 1. Instantaneous configuration of the particle-laden flow in (*a*) the one-way coupling, and (*b*) the two-way coupling. The contour plot represents the velocity magnitude normalised with the bulk velocities of the corresponding cases, $|\boldsymbol{u}|$. The particle population at $St_+ = 10$ is represented in both images (half of the domain is represented for the sake of clarity).

A summary of the dataset is listed in table 1. In all the simulations, the friction Reynolds number Re_* is fixed (same pressure drop), implying that the actual flow rate $Q = 2hU_b$ follows as a consequence of the fluid–particle momentum exchange. The simulation plan is designed to assess in a systematic way the role of the particle Stokes number and of the particle-to-fluid density ratio on the turbulence modification at fixed mass loading $\phi = 0.4$. For this purpose, the simulations are divided into two groups. In the first set of simulations, the Stokes number is changed at a fixed density ratio. The second set addresses the effect of the density ratio at fixed Stokes number. The mass loading is maintained constant by consistently adjusting the particle number N_p to compensate for the increase of the mass of each particle when the density ratio and/or the Stokes number are varied. The choice of the present parameters rules out the role of gravity in the dynamics of the particles. Indeed, the ratio between the particle terminal velocity v_t in a quiescent fluid and the bulk velocity can be expressed by $v_t/U_b = St_b/Fr_b^2$, where $Fr_b = U_b/\sqrt{gh}$ is the Froude number. In realistic conditions, i.e. in an actual experiment of air flowing in a channel of half-height $h = 1$ cm at the present value of the bulk Reynolds number, it turns out that $v_t/U_b \simeq 0.04$ in the worst scenario, i.e. for the particle population at $St_+ = 80$.

3. Results

The instantaneous channel flow configuration laden with the particle population at $St_+ = 10$ is reported in figure 1. Figure 1(*a*) pertains to the one-way coupling regime, and figure 1(*b*) pertains to the corresponding two-way coupling regime. The contour plot represents the fluid velocity magnitude normalised with the bulk velocity of the corresponding case. In the one-way regime, the fluid velocity is characterised by the presence of the ordered low- and high-speed streaks, whilst in the two-way regime, even though the streaky structure of the velocity field is still apparent, the spatial order is clearly altered. A related effect consists of the modification of the particle distribution. Indeed, ordered clusters are evident in figure 1(*a*), while they are hardly appreciable in figure 1(*b*). The analysis of the instantaneous flow configuration denotes an appreciable turbulence modification that is quantified and detailed below in terms of statistical observables.

974 A26-6

3.1. *Mean flow and friction coefficient*

The mean velocity profile is plotted in figure 2 for some selected relevant cases of table 1. Figures 2(*a,b*) show the effect of the Stokes number at a fixed density ratio in the semi-log scale and in the linear scale, respectively, the latter to better appreciate the modification of the flow rate. Particles with the largest St_+, e.g. $St_+ = 80$, have a small, though measurable, effect on the mean velocity profile that approaches the curve of the one-way coupling regime. When the Stokes number is decreased, the interphase momentum coupling becomes more effective, and the ensuing velocity profile departs from the reference data of the one-way coupled simulation. All the data show a sensible reduction of the flow speed that occurs up to the smallest Stokes number considered, $St_+ = 2$. By increasing the density ratio up to $\rho_p/\rho_f = 5760$ at a fixed Stokes number, the effect of the particles always results in a depletion of the velocity profile; see figures 2(*c,d*). Note that the depletion of the flow speed becomes progressively weaker, being the velocity profile for the case $\rho_p/\rho_f = 5760$ almost superimposed on the reference Newtonian case. This suggests a relevant role of the particle-to-fluid density ratio that must be taken into account when comparing different studies and flow configurations.

All the data reported in figure 2 indicate that the effect of the particles, at least in the range of parameters considered in this study, goes always in the direction of reducing the flow speed for a prescribed pressure gradient. This means that the laden flow experiences a larger friction drag than the unladen case. Figure 3 shows the ratio between the friction coefficient $C_f = 2\tau_w/(\rho_f U_b^2)$ and the friction coefficient of the reference uncoupled simulation $C_{f,0} = 2\tau_w/(\rho_f U_{b,0}^2)$. At large Stokes numbers, the ratio $C_f/C_{f,0}$ approaches a plateau; at intermediate Stokes numbers, a rapid increase of $C_f/C_{f,0}$ is measured when decreasing St_+; and at relatively smaller Stokes numbers, the increase of $C_f/C_{f,0}$ is weaker though still clear. For all the values of the particle-to-fluid density ratio, the drag result is always larger than the corresponding value measured in the uncoupled case. Indeed, $C_f/C_{f,0}$ starts constant, decreases with increasing particle-to-fluid density ratios to saturate eventually at very large values of ρ_p/ρ_f, being always above 1.

The particle average distribution is presented in figure 4 as a function of the wall-normal distance. The particle concentration is defined as $C(z) = (\langle n_p \rangle / \Delta V_x)/(N_p/V_f)$, where $\langle n_p \rangle$ is the average number of particles in a cylindrical shell of volume $\Delta V_z = L_x \times L_y \times \Delta_z$ placed at distance z from the wall, and N_p is the total number of particles in the fluid domain V_f. The normalisation is chosen such that $C = 1$ when the particles are distributed homogeneously throughout the fluid domain. Figure 4(*a*) documents the effect of the Stokes number, and figure 4(*b*) the effect of the density ratio. Note that particles cannot lie in a wall layer as thick as their radius.

Concerning the effect of the Stokes number, the particle feedback modifies the particle concentration with respect to the uncoupled case only for the populations at $St_+ = 2$ and $St_+ = 10$. At higher Stokes number ($St_+ = 80$), the particles are still unevenly distributed across the flow domain, but the difference between the one-way and two-way coupled simulations is less apparent. It turns out that the particle accumulation near the wall is not necessarily the only precursor for turbulence modification. Figure 4(*b*) addresses the effect of the density ratio. Note that all three two-way coupled cases correspond to a single one-way couple case since in the latter, only the Stokes number matters. These results prove that ρ_p/ρ_f is a crucial parameter in two-way coupled particle-laden flows, and that most of our understanding that is based on one-way coupled simulations must be reconsidered since the particle-to-fluid density ratio does not enter the uncoupled case dynamics.
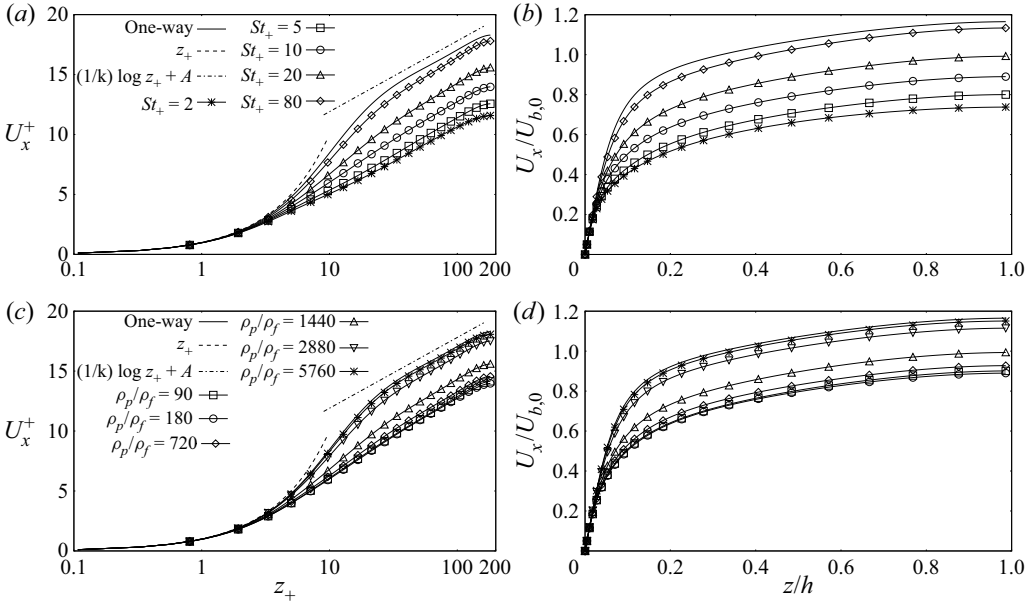
Figure 2. Mean streamwise velocity $U_x = \langle u \rangle$ versus the wall-normal distance z. (*a,c*) Data normalised with internal units, $U_x^+ = U_x/u_*$ against $z_+ = z/\ell_*$. (*b,d*) Data normalised with external units, $U_x/U_{b,0}$ against z/h. (*a,b*) Data at $\rho_p/\rho_f = 180$ and $\phi = 0.4$ for different Stokes numbers. (*c,d*) Data at fixed mass load $\phi = 0.4$ and Stokes number $St_+ = 10$ for different density ratios. The solid black line in all plots is the mean velocity profile in the one-way coupling regime. In (*a,c*), the log law with $k = 0.39$ and $A = 6$ (dash-dotted line), and the viscous scaling $U_x^+ = z_+$ (dotted line), are reported.
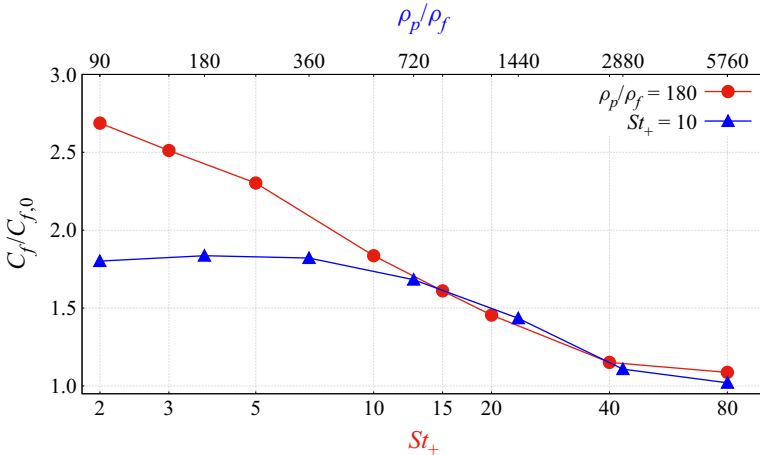
Figure 3. The friction coefficient C_f normalised with the friction coefficient $C_{f,0}$ in the one-way coupling regime (no back-reaction). Data are plotted versus the Stokes number St_+ for the dataset at a fixed density ratio $\rho_p/\rho_f = 180$ (bottom *x*-axis, red circles), and versus the density ratio ρ_p/ρ_f for the dataset at fixed Stokes number $St_+ = 10$ (top *x*-axis, blue triangles).

3.2. *Turbulent fluctuations*

The mean streamwise velocity fluctuation profile is shown in figure 5. Figure 5(*a*) addresses the role of the Stokes number, and figure 5(*b*) addresses the role of the density ratio. The striking effect observed in the two-way coupling regime consists of
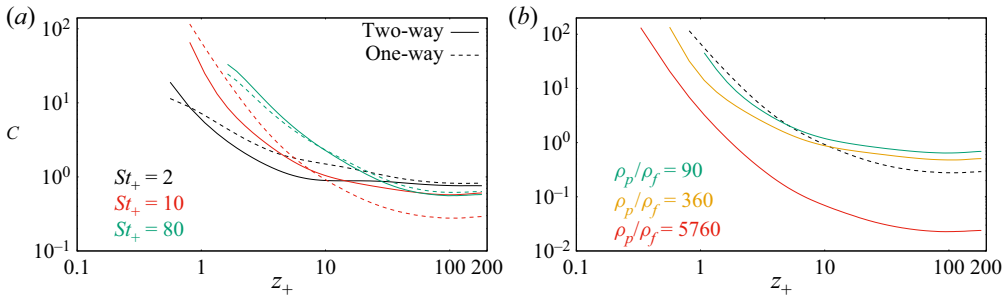
974 A26-8

Figure 4. Mean particle concentration versus wall normal distance $z_+ = z/\ell_*$. (*a*) Data at fixed $\rho_p/\rho_f = 180$ and $\phi = 0.4$ for different Stokes numbers. (*b*) Data at fixed $\phi = 0.4$ and $St_+ = 10$ for different density ratios. The solid lines correspond to the two-way coupling regime; the dashed colour-matched lines correspond to the one-way coupling regime.
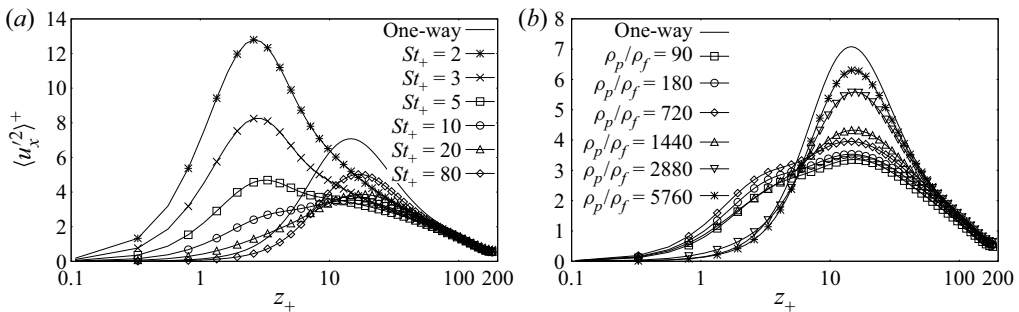

Figure 5. Mean streamwise velocity fluctuation $\langle u_x'^2 \rangle_+ = \langle u_x'^2 \rangle / u_*^2$ versus wall-normal distance $z_+ = z/\ell_*$. (*a*) Data at fixed $\rho_p/\rho_f = 180$ and $\phi = 0.4$ for different Stokes numbers. (*b*) Data at fixed $\phi = 0.4$ and $St_+ = 10$ for different density ratios. The solid black line in all plots corresponds to the one-way coupling regime.

the modification of turbulent fluctuations near the wall. Particles at large Stokes numbers $St_+ = 80$ and 20 deplete the peak intensity in the buffer layer and the lower part of the log layer. Besides the depletion in the buffer region, the particle at $St_+ = 10$ starts augmenting the fluctuations in the viscous sublayer. When the Stokes number is further decreased (see cases $St_+ \in [2, 5]$), a new peak of velocity fluctuations appears definitively in the viscous sublayer. Concerning the effect of the density ratio (figure 5*b*), the fluctuations in the viscous sublayer are augmented, while the reduction of the intensity peak in the buffer region is relevant up to $\rho_p/\rho_f = 1440$. In the highest density ratio $\rho_p/\rho_f = 5760$ case, the viscous sublayer is unaltered, while the peak of the fluctuations is still depleted in the buffer region.

Figure 6 presents the wall-normal mean velocity fluctuation profile. The two-way coupling effects are again striking in the near-wall region, where a clean peak is observed in the viscous sublayer for all the particle populations except for the case at $St_+ = 80$ where, instead, fluctuations are depleted across the entire channel height. The increase of the wall-normal velocity fluctuations is particularly evident for the populations at relatively small Stokes number, i.e. $St_+ \in [2, 5]$. Similar behaviour is observed for cases at different density ratios (see figure 6*b*), where the fluctuations approach the data of the one-way coupling regime only for the case at $\rho_p/\rho_f = 5760$.

Figure 7 shows Reynolds shear stress profile modification due to the particle presence. The Reynolds stresses are reduced in the log region and in the buffer region, to be
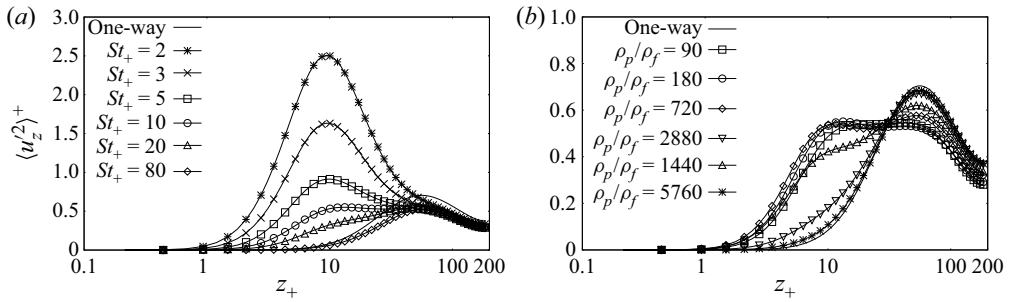
Figure 6. Mean wall-normal velocity fluctuation $\langle u_z'^2 \rangle_+ = \langle u_z'^2 \rangle / u_*^2$ versus wall-normal distance $z_+ = z/\ell_*$. (*a*) Data at fixed $\rho_p/\rho_f = 180$ and $\phi = 0.4$ for different Stokes numbers. (*b*) Data at fixed $\phi = 0.4$ and $St_+ = 10$ for different density ratios. The solid black line in all plots corresponds to the one-way coupling regime.
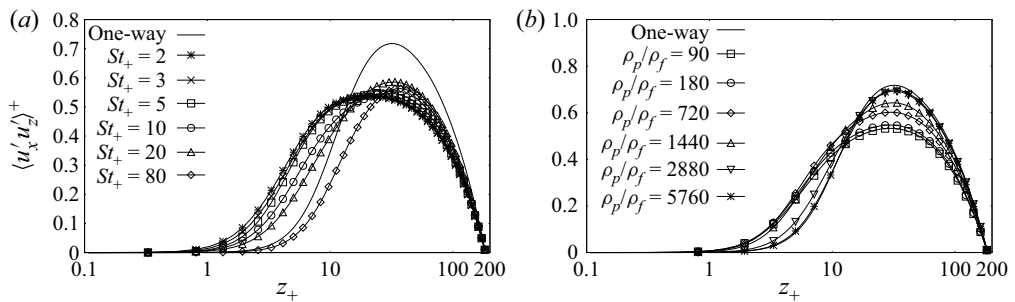

Figure 7. Mean Reynolds shear stress profile $\langle u_x' u_z' \rangle_+ = \langle u_x' u_z' \rangle / u_*^2$ versus wall-normal distance $z_+ = z/\ell_*$. (*a*) Data at fixed $\rho_p/\rho_f = 180$ and $\phi = 0.4$ for different Stokes numbers. (*b*) Data at fixed $\phi = 0.4$ and $St_+ = 10$ for different density ratios. The solid black line in all plots corresponds to the one-way coupling regime.

increased significantly in the viscous sublayer except for the population at $St_+ = 80$. Similar behaviour is observed when the density ratio is changed.

The augmentation of the Reynolds shear stresses close to the wall indicates an increase in the momentum transfer towards the wall due to turbulent fluctuations. The turbulent fluctuations in the viscous sublayer are augmented along both the streamwise and wall-normal directions, with also an alteration of the off-diagonal components of the stresses. One can figure out that when fast particles coming from the channel bulk approach the wall, due to their inertia, they have streamwise and wall-normal velocities much different to those of the surrounding fluid. The same happens for slow particles that from the near-wall region migrate towards the centre of the channel. It follows a large slip velocity between particles and fluid, resulting in an intense and localised momentum exchange that manifests as a large increment of fluctuations. This point is investigated more deeply by addressing stress balance.

3.3. *Stress balance*

The mean streamwise momentum balance,

$$\frac{\partial}{\partial z}\left[\mu\,\frac{\partial U_x}{\partial z} - \rho_f\langle u_x' u_z' \rangle + \tau_e\right] = \left.\frac{\mathrm{d}p}{\mathrm{d}x}\right|_0, \tag{3.1}$$

helps us to understand turbulence modification. In (3.1), $\tau_e = \int_0^z \langle f_x \rangle \, d\zeta$ is the extra stress due to the particles; see (2.2). After a first integration, the stress balance reads

$$\mu \frac{\partial U_x}{\partial z} - \rho_f \langle u_x' u_z' \rangle + \tau_e = \tau_w \left(1 - \frac{z}{h} \right), \tag{3.2}$$

where the mean pressure gradient has been replaced by the wall shear stress τ_w, being $-dp/dx|_0 = \tau_w/h$.

The viscous stress $\tau_\mu = \mu \, \partial U_x/\partial z$, the Reynolds shear stress $\tau_R = -\rho_f \langle u_x' u_z' \rangle$ and the extra stress τ_e are plotted in figure 8. The total stress $\tau_T = \tau_w(1 - z/h)$ and the Reynolds shear stress in the one-way coupling regime are shown in all plots for comparison. The interesting feature of the two-way coupled simulations is the contribution of the extra stress, which alters the overall balance; see also the results by Lee & Lee (2015) in the context of point-particle simulations, and Costa *et al.* (2021) in the context of resolved particle simulations. For relatively small Stokes number $St_+ \in [2, 20]$ (figures 8a–c), the extra stress represents a significant contribution to the balance both in the near-wall region and in the bulk of the flow. In the near-wall region, τ_e is comparable to or even larger than the corresponding Reynolds shear stress. Here, the extra stress provides an alternative way of transferring streamwise momentum towards the wall in synergy with the augmented Reynolds shear stress; see figure 7. Near the wall, the sum of the extra stress and the Reynolds shear stress turns out to be always larger than the Reynolds shear stress of the one-way coupled case. This behaviour provides a rational interpretation and explanation of the increased turbulent velocity fluctuations near the wall. It is also worth discussing the stress balance at the larger Stokes number $St_+ = 80$, where the contribution of the extra stress is still significant. However, Reynolds shear stress is depleted near the wall, and the sum of the two tends to match the Reynolds shear stress of the one-way coupling regime. This results in a negligible drag increase as observed in figure 3.

The effect of the density ratio is presented in figure 9. For the values of ρ_p/ρ_f up to 1440, a significant extra stress is present, with the sum of the extra stress and the Reynolds shear stress always larger than the Reynolds shear stress of the one-way coupling regime. This gives the reason for the significant increase in the friction drag. Only at the highest values $\rho_p/\rho_f = 2880$ (not shown) and $\rho_p/\rho_f = 5760$ does the extra stress, though still appreciable, get smaller, and the sum of the extra stress and the Reynolds shear stress approaches the Reynolds shear stress of the one-way coupling regime. Indeed, in these latter cases, the alteration of the overall friction drag is relatively small.

Further insight into turbulence modification can be gained from (3.2), which can be integrated in $[0, z]$ and in $[0, h]$ (Fukagata, Iwamoto & Kasagi 2002; Costantini, Mollicone & Battista 2018), leading to the global balance

$$\mu h U_b + \int_0^h (h - z) (\tau_R + \tau_e) \, dz = \frac{1}{3} \tau_w h^2. \tag{3.3}$$

Equation (3.3) expresses the fact that in a turbulent flow, only part of the available pressure drop, i.e. the wall shear stress, produces a flow rate U_b. Part of the pressure drop is absorbed by the turbulent Reynolds shear stresses, and in two-way coupling conditions, another part is absorbed by the particle extra stress. Equation (3.3) can be recast in dimensionless form as

$$3 \frac{Re_b}{Re_*^2} + 3 \int_0^1 (1 - \tilde{z}) (\tau_R^+ + \tau_e^+) \, d\tilde{z} = 1, \tag{3.4}$$
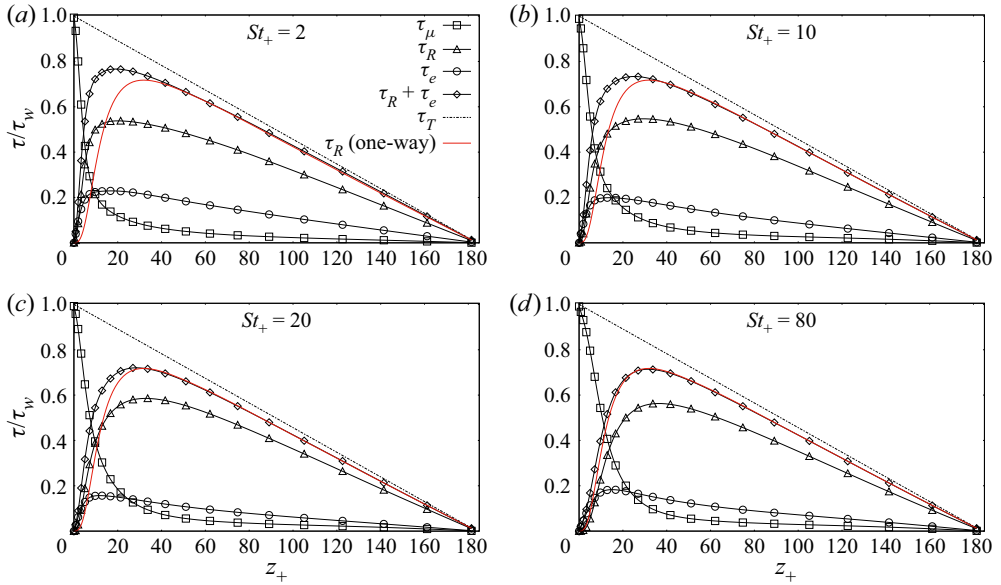
Figure 8. Mean stress balance (3.2) versus the wall-normal distance z_+. Viscous stress τ_μ ($\square$), Reynolds shear stress τ_R ($\triangle$), extra stress τ_e ($\bigcirc$), total turbulent stress $\tau_R + \tau_e$ ($\diamond$), total stress $(1 - z/h)$ (dash-dotted line), Reynolds shear stress τ_R in the one-way coupling regime (solid line). All stresses are normalised with the wall shear stress τ_w. In all plots, $\phi = 0.4$ and $\rho_p/\rho_f = 180$.
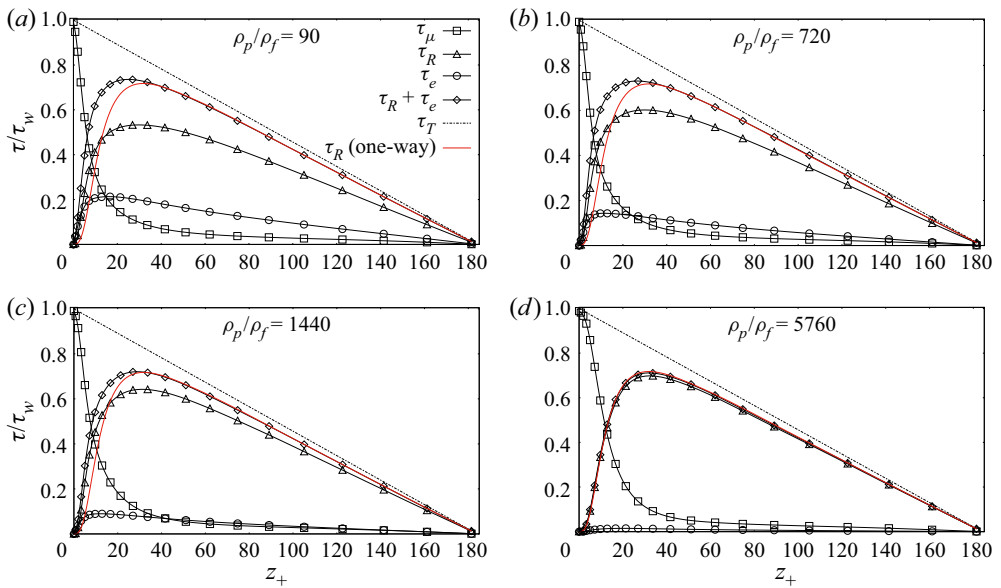

Figure 9. Mean stress balance (3.2) versus the wall-normal distance z_+. Viscous stress τ_μ ($\square$), Reynolds shear stress τ_R ($\triangle$), extra stress τ_e ($\bigcirc$), total turbulent stress $\tau_R + \tau_e$ ($\diamond$), total stress $(1 - z/h)$ (dash-dotted line), Reynolds shear stress τ_R in the one-way coupling regime (solid line). All stresses are normalised with the wall shear stress τ_w. In all plots, $\phi = 0.4$ and $St_+ = 10$.
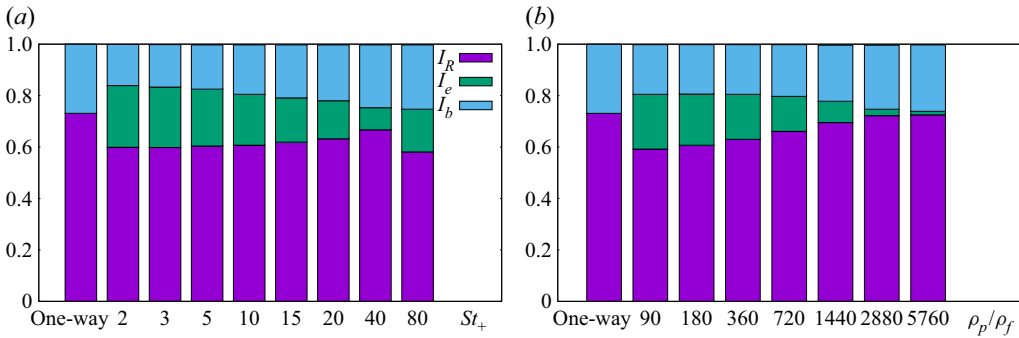
Figure 10. Mean flow rate budget (3.4), with $I_b = 3\,Re_b/Re_*^2$, $I_R = 3\int_0^1 (1 - \tilde{z})\tau_R^+ \,\mathrm{d}\tilde{z}$ and $I_e = 3\int_0^1 (1 - \tilde{z})\tau_e^+ \,\mathrm{d}\tilde{z}$. (*a*) Data at different Stokes numbers. (*b*) Data at different density ratios. The first bar in each plot shows the data of the one-way coupling case.

where $\tilde{z} = z/h$, and τ_R^+, τ_e^+ are the Reynolds shear stress and the particle extra stress expressed in wall units, respectively. Note that the contribution of the Reynolds shear stress and the extra stress is now weighted by $(1 - \tilde{z})$, meaning that the near wall values of the corresponding profiles contribute more significantly to the balance.

The different terms in the budget, $I_b = 3\,Re_b/Re_*^2$, $I_R = 3\int_0^1 (1 - \tilde{z})\tau_R^+ \,\mathrm{d}\tilde{z}$ and $I_e = 3\int_0^1 (1 - \tilde{z})\tau_e^+ \,\mathrm{d}\tilde{z}$, are shown in figure 10. Figure 10(*a*) highlights the effect of the Stokes number. In the $St_+ \in [2, 40]$ range, the portion of the pressure drop absorbed by the Reynolds shear stress and by the flow rate is depleted. The extra stress contribution absorbs the remaining part of the available pressure drop, which represents a significant part of the balance. At the largest Stokes number $St = 80$, the extra stress and the (depleted) Reynolds stress turn out to reproduce the turbulence stress contribution of the uncoupled case, thus leaving almost unaltered the flow rate contribution. Note that a significant increase in the friction drag starts occurring at $St_+ = 20$, corresponding to a bulk Stokes number $St_b = 1.7 \sim O(1)$ (see figure 3), in correspondence with an appreciable contribution of I_e in the budget. Finally, the total turbulent stress contribution $I_R + I_e$ turns out to be always larger than the value of the uncoupled case to eventually reach the one-way coupling regime at $St_+ = 80$. As ρ_p/ρ_f is increased, the terms in the budget approach the corresponding values of the one-way coupling regime in a monotonic way, making I_e progressively smaller; see figure 10(*b*).

3.4. *Turbulent kinetic energy*

The TKE budget reads

$$\nabla \cdot \boldsymbol{\Phi} = \Pi - \varepsilon + \Pi_p, \tag{3.5}$$

where $\boldsymbol{\Phi}$ is the TKE spatial energy flux vector, $\Pi = -\langle u'_x u'_z\rangle\,\partial U_x/\partial z$ is the production term, $\varepsilon = 1/Re_b\,\langle \partial_i u'_j\,\partial_i u'_j\rangle$ is the viscous energy pseudo-dissipation rate, and $\Pi_p = \langle f'_i u'_i\rangle$ is the extra production/destruction term due to the particles' feedback on the fluid. Given the flow symmetries, the only relevant derivative in the divergence term is along the wall-normal direction z. This selects the z component of the flux vector, $\Phi_z = 1/2\langle u'_i u'_i u'_z\rangle + \langle p' u'_z\rangle - 1/Re_b\,\partial k_t/\partial z$, that encompasses turbulent transport, pressure diffusion and viscous diffusion, respectively, with $k_t = 1/2\langle u'_i u'_i\rangle$ the TKE.

The production term Π and the extra term due to particles Π_p are shown in figure 11 for cases at different Stokes numbers and density ratios (the production term of the one-way
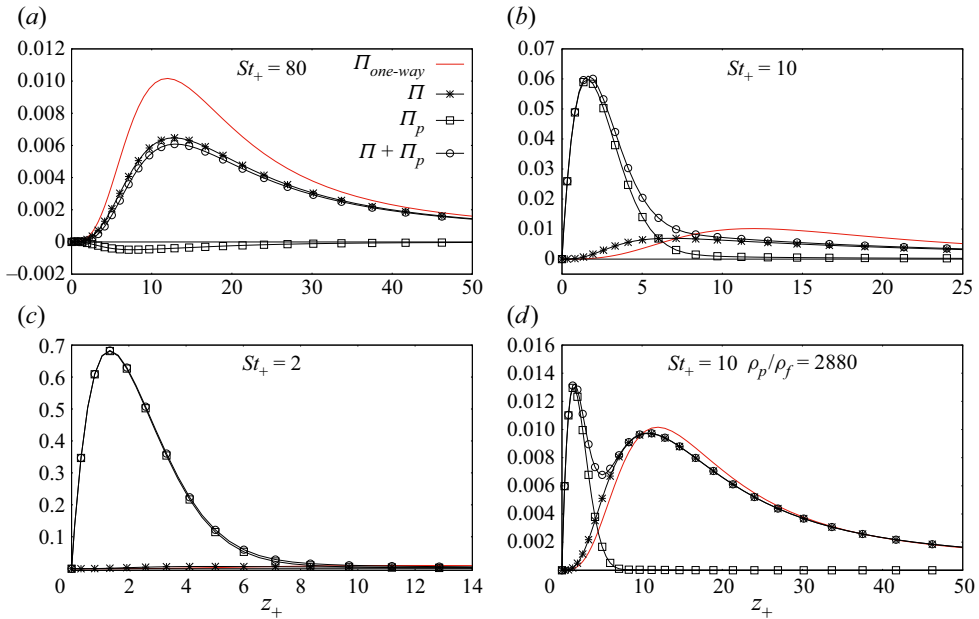
Figure 11. Turbulent kinetic energy production Π ($*$), extra production/destruction term Π_p ($\square$) and their sum $\Pi + \Pi_p$ ($\bigcirc$) versus the wall normal distance z_+, for (a) $St_+ = 80$, (b) $St_+ = 10$, (c) $St_+ = 2$, and (d) $St_+ = 10$ and $\rho_p/\rho_f = 2880$. In all the plots, the production term $\Pi_{one\text{-}way}$ in the one-way coupling regime (solid line) is reported for comparison.

coupling case is reported for comparison). The data at $St_+ = 80$ show how the particles deplete the TKE production but do not shift its peak position since the particles turn out to behave as a sink of TKE. This contributes to a further reduction of the effective TKE production $\Pi + \Pi_p$. The behaviour changes dramatically for particle populations at small Stokes number, where a significant increase of the friction drag occurs. The particles at $St_+ = 10$ (figure 11b) can deplete the production term Π and shift its peak close to the wall. The striking effect concerns the particle term Π_p, which behaves as a source of TKE near the wall. At small z_+, the term Π_p is larger in its amplitude than the turbulent production Π. This behaviour is even more pronounced for the population at $St_+ = 2$ (figure 11c), where the particle term Π_p largely overwhelms the production term Π, providing a localised source of TKE in the viscous sublayer (note that the plot is on a different scale, one order of magnitude larger than in the other plots). Finally, figure 11(d) addresses the effect of the density ratio reporting the data at $\rho_p/\rho_f = 2880$ (see also figure 11b). The particle term Π_p is still comparable in amplitude with Π. The effective production $\Pi + \Pi_p$ has two peaks, one in the buffer layer and one in the viscous sublayer induced by the particles.

The dramatic alteration of the effective production $\Pi + \Pi_p$ impacts the energy flux vector that spatially redistributes the TKE. In figure 12, the flux vector $\boldsymbol{\Phi}$ is superimposed on the contour plot of the effective source $Q = \Pi - \varepsilon + \Pi_p$ (either positive or negative). The sign of Q fixes the value of $\nabla \cdot \boldsymbol{\Phi}$ and the ensuing direction of the flux vector. In principle, $\boldsymbol{\Phi} = \Phi_z \boldsymbol{e}_z + \Phi_x \boldsymbol{e}_x$, where $\Phi_x = U_x k_t + 1/2\langle u'_i u'_i u'_x \rangle + \langle p' u'_x \rangle$ (not shown) is responsible for the downstream transport of the energy and does not contribute to the flux divergence. The vector $\Phi_z \boldsymbol{e}_z$ is shown along the vertical axis of each plot, in arbitrary units:

974 A26-14
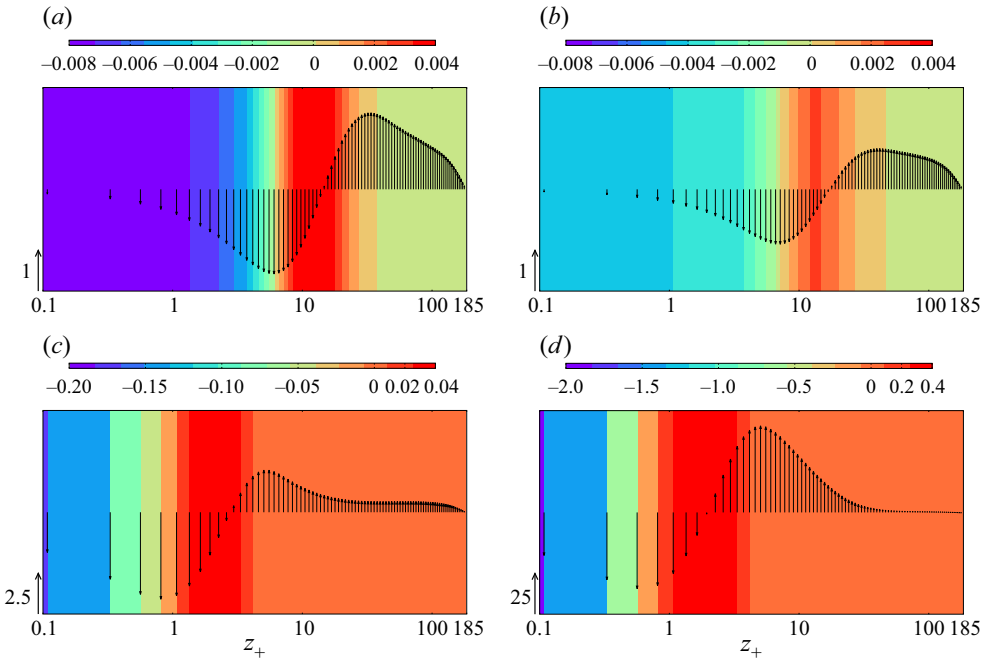
Figure 12. Contour plot of the effective TKE source $Q = \Pi - \varepsilon + \Pi_p$. The vectors represent flux vector $\Phi_z(z)\,\boldsymbol{e}_z$ in arbitrary though comparable units reported in the bottom left corner of each plot. (*a*) One-way coupling; (*b–d*) two-way coupled cases at $St_+ = 80$, 10 and 2, respectively.

the vertical arrow in the bottom left corner of each plot reports the direction and the value of the selected units to make a fair comparison among the different cases.

Figure 12(*a*) pertains to the one-way coupling regime. The effective source Q is positive in the buffer layer (locally $\Pi > \varepsilon$). This triggers the spatial fluxes directed towards the channel's centre and towards the wall. The flux directed towards the centre of the channel crosses (with slight modifications) the log layer, and is eroded progressively by viscosity in the bulk, where the effective source is mildly negative in a wide range of z_+. More interesting is the behaviour of the flux directed towards the wall. The wall itself behaves as an intense sink of energy (see (3.5)) evaluated at the wall, $\partial_z\phi_z|_{z=0} = -\varepsilon|_{z=0}$ (Pope 2000). The flux is eroded in about 5 wall units, and the effective source Q quickly becomes negative approaching the wall. The same energy path is observed for the particle population at $St_+ = 80$ (figure 12*b*), but with reduced amplitude.

The situation changes dramatically at smaller Stokes numbers, i.e. $St_+ = 10$ and 2; see figures 12(*c,d*). The effective source Q is strongly altered by the particle contribution Π_p. The range of positive values of Q is shifted in the viscous sublayer, and its intensity is increased progressively with decreasing St_+. The spatial flux originates closer to the wall, and its intensity gets larger and larger at decreasing St_+, since the effective production is located in the viscous sublayer, and its intensity is dominated by the particle contribution Π_p. This triggers an intense spatial flux towards the wall that is eroded rapidly by viscous dissipation in about one wall unit. This behaviour gives a rational reason for the increased friction drag. The other part of the flux directed towards the centre of the channel is comparable in intensity with the flux directed towards the wall. Indeed, it triggers the large velocity fluctuations observed in the viscous sublayer (see figures 5 and 6), and is

eroded progressively by viscosity moving towards the centre of the channel, where the effective source is mildly negative in a wide range of z_+.

4. Final remarks

Direct numerical simulations of a particle-laden turbulent channel flow in the two-way coupling regime have been discussed to characterise and explain the turbulence modulation in a wide region of the parameter space. The particle Stokes number is varied in the range $St_+ \in [2, 80]$, and the particle-to-fluid density ratio in the range $\rho_p/\rho_f \in [90, 5760]$ at fixed mass loading $\phi = 0.4$. The interphase momentum coupling has been modelled using the ERPP approach, which, by overcoming at once many drawbacks of the particle-source in cell method, also allows the exploration of a wide region of the parameter space.

For all the cases considered, the friction drag was always found to be augmented by the particles' back-reaction with respect to the reference unladen case. The flow rate is reduced substantially by reducing the Stokes number to $St_+ = 2$, the smallest value considered. An appreciable alteration of the friction drag, say 10 % of the friction drag in the unladen case, occurs for particle populations characterised by a bulk Stokes number $St_b = O(1)$. The present simulations show that a measurable increase in the drag persists for a wide range of density ratios. Only the extreme case at $\rho_p/\rho_f = 5760$ does not show such friction drag increase. The velocity fluctuation intensities are also altered by two-way coupling effects. At small Stokes numbers, a new peak of fluctuations appears in the viscous sublayer, and its amplitude is almost twice the peak intensity in the unladen case for the particle population at $St_+ = 2$. The modification of the turbulence structure has been explained by addressing the mean stress balance and the turbulent kinetic energy (TKE) budget. In terms of stresses, the particles contribute with the extra stress that represents an alternative path for the streamwise momentum to be transferred towards the wall. Even though the Reynolds shear stress is depleted in the bulk of the flow, its intensity is augmented in the viscous sublayer. However, the total effective turbulent stress $\tau_R + \tau_e$ is augmented with respect to the one-way coupling regime, leading to an enhanced momentum mixing and thus larger friction. The TKE budget highlights the modification of the spatial energy fluxes across the channel height. For cases where a substantial increase of the friction drag is observed, the production/destruction term due to the particles Π_p overwhelms the classical mechanisms of TKE production via the Reynolds shear stresses Π close to the wall. The TKE is produced by the particles in the viscous sublayer, and the ensuing energy spatial fluxes are enhanced. The spatial flux directed towards the wall is eroded rapidly by viscous dissipation within a few wall unit distances from the wall, giving the reason for the enhanced dissipation at the wall, i.e. the drag increase.

Author ORCIDs.
  P. Gualtieri https://orcid.org/0000-0001-5121-4234;
  F. Battista https://orcid.org/0000-0001-5634-5663;

F. Salvadore https://orcid.org/0000-0002-1829-3388;

C.M. Casciola https://orcid.org/0000-0001-8795-4517.

REFERENCES

AKIKI, G., JACKSON, T.L. & BALACHANDAR, S. 2017*a* Pairwise interaction extended point-particle model for a random array of monodisperse spheres. *J. Fluid Mech.* **813**, 882–928.

AKIKI, G., MOORE, W.C. & BALACHANDAR, S. 2017*b* Pairwise-interaction extended point-particle model for particle-laden flows. *J. Comput. Phys.* **351**, 329–357.

BALACHANDAR, S. & EATON, J.K. 2010 Turbulent dispersed multiphase flow. *Annu. Rev. Fluid Mech* **42**, 111–133.

BALACHANDAR, S., LIU, K. & LAKHOTE, M. 2019 Self-induced velocity correction for improved drag estimation in Euler–Lagrange point-particle simulations. *J. Comput. Phys.* **376**, 160–185.

BATTISTA, F., MOLLICONE, J.-P., GUALTIERI, P., MESSINA, R. & CASCIOLA, C.M. 2019 Exact regularised point particle (ERPP) method for particle-laden wall-bounded flows in the two-way coupling regime. *J. Fluid Mech.* **878**, 420–444.

BRANDT, L. & COLETTI, F. 2022 Particle-laden turbulence: progress and perspectives. *Annu. Rev. Fluid Mech.* **54**, 159–189.

CAPECELATRO, J. & DESJARDINS, O. 2013 An Euler–Lagrange strategy for simulating particle-laden flows. *J. Comput. Phys.* **238**, 1–31.

CAPECELATRO, J., DESJARDINS, O. & FOX, R.O. 2018 On the transition between turbulence regimes in particle-laden channel flows. *J. Fluid Mech.* **845**, 499.

CAPECELATRO, J., PEPIOT, P. & DESJARDINS, O. 2014 Numerical characterization and modeling of particle clustering in wall-bounded vertical risers. *Chem. Engng J.* **245**, 295–310.

CHORIN, A.J. 1968 Numerical solution of the Navier–Stokes equations. *Math. Comput.* **22** (104), 745–762.

COSTA, P., BRANDT, L. & PICANO, F. 2020 Interface-resolved simulations of small inertial particles in turbulent channel flow. *J. Fluid Mech.* **883**, A54.

COSTA, P., BRANDT, L. & PICANO, F. 2021 Near-wall turbulence modulation by small inertial particles. *J. Fluid Mech.* **922**, A9.

COSTANTINI, R., MOLLICONE, J.-P. & BATTISTA, F. 2018 Drag reduction induced by superhydrophobic surfaces in turbulent pipe flow. *Phys. Fluids* **30** (2), 025102.

CROWE, C.T., SHARMA, M.P. & STOCK, D.E. 1977 The particle-source in cell method for gas droplet flow. *J. Fluid Engng* **99**, 325.

ELGOBASHI, S. 2006 An updated classification map of particle-laden turbulent flows. In *IUTAM Symposium on Computational Approaches to Multiphase Flow*, pp. 3–10. Springer.

EVRARD, F., DENNER, F. & VAN WACHEM, B. 2021 Quantifying the errors of the particle-source-in-cell Euler–Lagrange method. *Intl J. Multiphase Flow* **135**, 103535.

FONG, K.O., AMILI, O. & COLETTI, F. 2019 Velocity and spatial distribution of inertial particles in a turbulent channel flow. *J. Fluid Mech.* **872**, 367–406.

FU, W., LI, H., LUBOW, S., LI, S. & LIANG, E. 2014 Effects of dust feedback on vortices in protoplanetary disks. *Astrophys. J. Lett.* **795** (2), L39.

FUKAGATA, K., IWAMOTO, K. & KASAGI, N. 2002 Contribution of Reynolds stress distribution to the skin friction in wall-bounded flows. *Phys. Fluids* **14** (11), L73–L76.

GARG, R., NARAYANAN, C., LAKEHAL, D. & SUBRAMANIAM, S. 2007 Accurate numerical estimation of interphase momentum transfer in Lagrangian–Eulerian simulations of dispersed two-phase flows. *Intl J. Multiphase Flow* **33** (12), 1337–1364.

GATIGNOL, R. 1983 The Faxén formulas for a rigid particle in an unsteady non-uniform Stokes flow. *J. Méc. Théor. Appl.* **2** (2), 143–160.

GUALTIERI, P., BATTISTA, F. & CASCIOLA, C.M. 2017 Turbulence modulation in heavy-loaded suspensions of tiny particles. *Phys. Rev. Fluids* **2** (3), 034304.

GUALTIERI, P., PICANO, F., SARDINA, G. & CASCIOLA, C.M. 2015 Exact regularized point particle method for multiphase flows in the two-way coupling regime. *J. Fluid Mech.* **773**, 520–561.

HORWITZ, J.A.K. & MANI, A. 2016 Accurate calculation of Stokes drag for point-particle tracking in two-way coupled flows. *J. Comput. Phys.* **318**, 85–109.

IRELAND, P.J. & DESJARDINS, O. 2017 Improving particle drag predictions in Euler–Lagrange simulations with two-way coupling. *J. Comput. Phys.* **338**, 405–430.

JENNY, P., ROEKAERTS, D. & BEISHUIZEN, N. 2012 Modeling of turbulent dilute spray combustion. *Prog. Energy Combust. Sci.* **38** (6), 846–887.

KLEINSTREUER, C. & ZHANG, Z. 2010 Airflow and particle transport in the human respiratory system. *Annu. Rev. Fluid Mech.* **42**, 301–334.

LEE, J. & LEE, C. 2015 Modification of particle-laden near-wall turbulence: effect of Stokes number. *Phys. Fluids* **27** (2), 023303.

LI, J., WANG, H., LIU, Z., CHEN, S. & ZHENG, C. 2012 An experimental study on turbulence modification in the near-wall boundary layer of a dilute gas-particle channel flow. *Exp. Fluids* **53** (5), 1385–1403.

LOMHOLT, S. & MAXEY, M.R. 2003 Force-coupling method for particulate two-phase flow: Stokes flow. *J. Comput. Phys.* **184** (2), 381–405.

MARCHIOLI, C., PICCIOTTO, M. & SOLDATI, A. 2007 Influence of gravity and lift on particle velocity statistics and transfer rates in turbulent vertical channel flow. *Intl J. Multiphase Flow* **33** (3), 227–251.

MAXEY, M.R. & PATEL, B.K. 2001 Localized force representations for particles sedimenting in Stokes flow. *Intl J. Multiphase Flow* **27** (9), 1603–1626.

MAXEY, M.R. & RILEY, J.J. 1983 Equation of motion for a small rigid sphere in a nonuniform flow. *Phys. Fluids* **26**, 2437.

PAKSERESHT, P., ESMAILY, M. & APTE, S.V. 2020 A correction scheme for wall-bounded two-way coupled point-particle simulations. *J. Comput. Phys.* **420**, 109711.

PAN, Y. & BANERJEE, S. 1997 Numerical investigation of the effects of large particles on wall-turbulence. *Phys. Fluids* **9** (12), 3786–3807.

POPE, S.B. 2000 *Turbulent Flows*. Cambridge University Press.

POUSTIS, J.-F., SENONER, J.-M., ZUZIO, D. & VILLEDIEU, P. 2019 Regularization of the Lagrangian point force approximation for deterministic discrete particle simulations. *Intl J. Multiphase Flow* **117**, 138–152.

PROSPERETTI, A. 2015 Life and death by boundary conditions. *J. Fluid Mech.* **768**, 1–4.

RICHTER, D.H. 2015 Turbulence modification by inertial particles and its influence on the spectral energy budget in planar Couette flow. *Phys. Fluids* **27** (6), 063304.

RIGHETTI, M. & ROMANO, G.P. 2004 Particle–fluid interactions in a plane near-wall turbulent flow. *J. Fluid Mech.* **505**, 93–121.

SARDINA, G., SCHLATTER, P., BRANDT, L., PICANO, F. & CASCIOLA, C.M. 2012 Wall accumulation and spatial localization in particle-laden wall flows. *J. Fluid Mech.* **699**, 50–78.

SOLDATI, A. & MARCHIOLI, C. 2009 Physics and modelling of turbulent particle deposition and entrainment: review of a systematic study. *Intl J. Multiphase flow* **35** (9), 827–839.

VREMAN, A.W. 2007 Turbulence characteristics of particle-laden pipe flow. *J. Fluid Mech.* **584**, 235–279.

WOODS, W.A. 2010 Turbulent plumes in nature. *Annu. Rev. Fluid Mech.* **42**, 391–412.

YEO, K. & MAXEY, M.R. 2010 Simulation of concentrated suspensions using the force-coupling method. *J. Comput. Phys.* **229** (6), 2401–2421.

ZHAO, L.H., ANDERSSON, H.I. & GILLISSEN, J.J. 2010 Turbulence modulation and drag reduction by spherical particles. *Phys. Fluids* **22** (8), 081702.